Article:
Karakatsanis, NA, Abgral, R, Trivieri, MG et al. (2020) Hybrid PET- and MR-driven attenuation correction for enhanced ^{18}F-NaF and ^{18}F-FDG quantification in cardiovascular PET/MR imaging. Journal of Nuclear Cardiology, 27 (4). pp. 1126-1141. ISSN: 1071-3581

https://doi.org/10.1007/s12350-019-01928-0

Hybrid PET- and MR-driven attenuation correction for enhanced ^{18}F-NaF and ^{18}F-FDG quantification in cardiovascular PET/MR imaging

Nicolas A. Karakatsanis[1,2], Ronan Abgral[1,3], Maria Giovanna Trivieri[1], Marc R. Dweck[1,4], Philip M. Robson[1], Claudia Calcagno[1], Gilles Boeykens[1,5], Max L. Senders[1,5], Willem J. M. Mulder[1,5], Charalampos Tsoumpas[1,6], Zahi A. Fayad[1]

[1] Biomedical Engineering and Imaging Institute, Icahn School of Medicine at Mount Sinai, New York, NY, USA

[2] Department of Radiology, Weill Cornell Medical College, Cornell University, New York, NY, USA

[3] Department of Nuclear Medicine, University Hospital of Brest, Brest, France

[4] British Heart Foundation, Centre for Cardiovascular Science, University of Edinburgh, Edinburgh, United Kingdom

[5] Department of Medical Biochemistry, Academic Medical Center, Amsterdam, the Netherlands

[6] Biomedical Imaging Science Department, Leeds Institute of Cardiovascular and Metabolic Medicine, University of Leeds, Leeds, United Kingdom

Corresponding Author: Dr. Nicolas A. Karakatsanis, Biomedical Engineering and Imaging Institute, Icahn School of Medicine at Mount Sinai, 1470 Madison Ave, New York, NY, 10029

E-mail: nak2032@med.cornell.edu, Tel: 212-746-3454, Fax 212-746-4189

Running title: PET/MR data driven AC in cardiovascular imaging

Abbreviations: PET: Positron Emission Tomography**,** MR: Magnetic Resonance**,** ^{18}F-NaF: 18Fluoride-Sodium Fluoride**,** ^{18}F-FDG: 18Fluoride-Fluorodeoxyglucose, AC: attenuation correction, K_i: uptake rate constant, TBR: target-to-background ratio

Conflict of Interest and funding sources: This study was funded by the National Institutes of Health, National Heart, Lung and Blood Institute (NIH/NHLBI R01HL071021). All authors declare that they have no conflict of interest.

Authorship: N.A.K., M.R.D., C.T. and Z.A.F. have contributed to the conception and design of the presented study. N.A.K., R.A., C.C., G.B., M.L.S. and W.J.M.M. have participated in the preparation of the rabbit subjects and the preclinical PET/MR data acquisition and analysis. N.A.K., R.A., M.R.D., M.G.T., P.M.R. and Z.A.F. participated in the acquisition and analysis of the clinical PET/MR data N.A.K. coordinated the analysis and drafting of the manuscript. Z.A.F. is the principal investigator of the NIH grant R01 HL071021. Finally, all authors declare that they have participated in data collection, analysis and interpretation, as well as in the writing and revision of the manuscript and have all approved the submitted version.

Abstract

Background: The standard MR Dixon-based attenuation correction (AC) method in Positron Emission Tomography / Magnetic Resonance (PET/MR) imaging segments only the air, lung, fat and soft-tissues (4-class), thus neglecting the highly attenuating bone tissues and affecting quantification in bones and adjacent vessels. We sought to address this limitation by utilizing the distinctively high bone uptake rate constant K_i expected from ^{18}F-Sodium Fluoride (^{18}F-NaF) to segment bones from PET data and support 5-class hybrid PET/MR-driven AC for ^{18}F-NaF and ^{18}F-Fluorodeoxyglucose (^{18}F-FDG) PET/MR cardiovascular imaging.

Methods: We introduce 5-class K_i/MR-AC for (i) ^{18}F-NaF studies where the bones are segmented from Patlak K_i images and added as the 5th tissue class to the MR-Dixon 4-class AC map. Furthermore, we propose two alternative dual-tracer protocols to permit 5-class K_i/MR-AC for (ii) ^{18}F-FDG-only data, with a streamlined simultaneous administration of ^{18}F-FDG and ^{18}F-NaF at 4:1 ratio (R4:1), or (iii) for ^{18}F-FDG-only or both ^{18}F-FDG and ^{18}F-NaF dual-tracer data, by administering ^{18}F-NaF 90 min after an equal ^{18}F-FDG dosage (R1:1). The K_i-driven bone segmentation was validated against Computed Tomography (CT)-based segmentation in rabbits, followed by PET/MR validation on 108 vertebral bone and carotid wall regions in 16 human volunteers with and without prior indication of carotid atherosclerosis disease (CAD).

Results: In rabbits, we observed similar (<1.2% mean difference) vertebral bone ^{18}F-NaF SUV_{mean} scores when applying 5-class AC with K_i-segmented bone (5-class K_i/CT-AC) versus CT-segmented bone (5-class CT-AC) tissue. Considering the PET data corrected with continuous CT-AC maps as gold-standard, the percentage SUV_{mean} bias was reduced by 17.6% (^{18}F-NaF) and 15.4% (R4:1) with 5-class K_i/CT-AC versus 4-class CT-AC. In humans without prior CAD indication, we reported 17.7% and 20% higher ^{18}F-NaF target-to-background ratio (TBR) at carotid bifurcations wall and vertebral bones, respectively, with 5- versus 4-class AC. In the R4:1 human cohort, the mean ^{18}F-FDG TBR increased by 12.2% at carotid bifurcations wall and 19.9% at vertebral bones. For the R1:1 cohort of human without CAD indication, mean TBR increased by 15.3% (^{18}F-FDG) and 15.5% (^{18}F-NaF) at carotid bifurcations and 21.6% (^{18}F-FDG) and 22.5% (^{18}F-NaF) at vertebral bones. Similar TBR enhancements were observed whe applying the proposed AC method to human subjects with prior CAD indication..

Conclusions: K_i-driven bone segmentation and 5-class hybrid PET/MR-driven AC is feasible and can significantly enhance ^{18}F-NaF and ^{18}F-FDG contrast and quantification in bone tissues and carotid walls.

Keywords: PET/MR, carotid, bone segmentation, attenuation correction, ^{18}F-NaF, ^{18}F-FDG

Introduction

Positron Emission Tomography (PET) has enabled the in-vivo quantitative imaging of numerous radio-pharmaceutical tracers by time-coincidentally detecting two emitted gamma photons travelling through tissue in opposite directions (1, 2). However, the photons may be absorbed or scattered before reaching the detectors resulting in PET signal attenuation, which is quantified by the attenuation coefficients (ACFs) (1, 3). Attenuation correction (AC) can be performed by estimating the tissue ACFs distribution, known as AC maps. Hybrid PET and Computed Tomography (CT) systems allow the estimation of highly-accurate CT-based AC (CT-AC) maps for superior PET quantification (4, 5). Nevertheless, PET/CT detectability may be limited for some lesions due to CT's low soft-tissue contrast (6).

Simultaneous PET and Magnetic Resonance (MR) systems have recently enabled the co-registration of PET images of highly specific molecular activity with multi-parametric MR images of superior soft-tissue resolution (7-9). Yet MR-based AC (MR-AC) may not be as accurate as CT-AC, due to MR's inherent limitations in ACFs quantification, especially for highly attenuating tissues, such as cortical bones (10-12). Currently, PET/MR scanners employ MR-Dixon sequences to segment all tissues into four classes, namely air, lungs, fat and soft-tissues, each assigned a discrete ACF value (13). Thus, the bones are notably neglected in 4-class MR-AC leading to PET quantification errors in adjacent-to-bone regions (12).

Recently, atlas-based segmentation methods enabled bone ACF estimation by registering bone atlases from past human studies (14, 15). However, this approach has limitations due to potential misregistrations and quantitative errors between the atlas and the current subject's actual bone ACF distribution (16). Alternatively, bone AC maps can be estimated from special MR sequences, such as ultra-short echo time (17), which require additional scan time and may not be uniformly accurate across different bone tissue types (18). To address these limitations, bone segmentation can instead be guided by ^{18}F-Sodium Fluoride (^{18}F-NaF) net uptake rate constant (K_i), which has been associated with distinctively higher values at bones, compared to the standardized uptake value (SUV) (19, 20).

In this study, we introduce a novel hybrid PET- and MR-driven 5-class AC method to segment cortical bone tissues from the generalized Patlak (gPatlak) K_i images (21, 22), as estimated from dynamic ^{18}F-NaF or dual-tracer ^{18}F-FDG:^{18}F-NaF PET data (23), while employing the 4-class MR Dixon-based segmentation for the remaining 4 tissue classes (13). Unlike standard Patlak, which assumes irreversible uptake, the gPatlak method accounts for the likelihood of mildly reversible radiotracer uptake in tissue to more accurately estimate K_i in bones (21, 22). We hypothesize that PET K_i-driven bone segmentation is clinically feasible and can be robustly employed to significantly improve PET

lesions quantification at bones or adjacent carotid arteries in PET/MR using ^{18}F-NaF and ^{18}F-FDG, which are two established radiotracers in cardiovascular imaging (24-29).

Materials and Methods

Initially, the proposed 5-tissue class hybrid PET/MR-AC framework was (i) streamlined for dynamic ^{18}F-NaF PET/MR protocols. Later, to extend its application to the well-established ^{18}F-FDG tracer, we also introduced two dual-tracer dynamic ^{18}F-FDG:^{18}F-NaF PET/MR protocols involving either (ii) the nearly simultaneous injection of the two compounds at an optimal 4:1 dosage ratio (R4:1), which aims at the AC of the ^{18}F-FDG distribution only, or (iii) the delayed ^{18}F-NaF administration 90 min after an equal ^{18}F-FDG dosage (R1:1), to support the independent AC of either compound (Fig. 1). (30). The total administered dosage in all three protocols is the same following the clinical guidelines (31).

Hybrid PET/MR-AC for ^{18}F-NaF PET/MR studies

The first protocol involved administering ^{18}F-NaF followed by a 90 min list-mode PET acquisition to track ^{18}F-NaF concentration in blood (input function, IF) and tissues (Fig. 1a, 1st row). The list-mode data was then histogrammed into 12×10 sec, 12×20 sec, 6×60 sec, 4×120 sec and 14×300 sec frames followed by Ordered Subsets – Expectation Maximization iterative reconstruction (4 iterations, 21 subsets) with a 4-class MR-AC map (13). The time-activity curves at every voxel $C(t)$, and the IF $C_p(t)$ were then fitted to the gPatlak model (Eq. 1) using a Basis Function Method to obtain parametric images of K_i, total blood distribution volume V and reverse uptake rate constant k_{loss} (22). Subsequently, the bones were segmented from the K_i image by setting a bottom threshold (Fig. 1d left).

$$\boldsymbol{C(t) = K_i \int_0^t C_p(\tau) e^{-k_{loss}(t-\tau)} d\tau + V C_p(t)} \qquad \textbf{(1)}$$

In all protocols, a fixed K_i bottom threshold of 0.001 mL/g/min was used to segment the human bone tissues. Moreover, a bottom threshold of SUV=2 was employed on the static ^{18}F-NaF images, 60-90 min post injection (p.i.), as an alternative segmentation criterion (20) and the resulting masks were compared against the K_i-segmented bone masks.

Meanwhile, the standard MR-Dixon-based 4-class MR-AC map was built by assigning a discrete ACF value (cm^{-1}) to each class: 0 (air), 0.021 (lungs), 0.086 (fat) and 0.1 (soft-tissues) (32). The K_i-segmented bone mask was later

added as the 5th tissue class (bone ACF=0.12 cm^{-1}) (32) to build the 5-class K_i/MR-AC map which was used by a new image reconstruction to produce the final PET image.

Hybrid PET/MR-AC for ^{18}F-FDG PET with nearly simultaneous ^{18}F-FDG:^{18}F-NaF administration

In order to apply the 5-class K_i/MR-AC method to ^{18}F-FDG studies, we introduced a second PET/MR scan protocol involving the nearly simultaneous administration, within a 3-5 minute interval, of the ^{18}F-FDG and ^{18}F-NaF compounds, followed by a 90min list-mode PET/MR acquisition (Fig. 1b) (23). Although simultaneous injection can be easier adopted in clinic, it may hamper the discrimination between the two tracers in regions of common uptake, due to potentially similar kinetics. This protocol was therefore designed for PET studies aiming at ^{18}F-FDG uptake evaluations with the ^{18}F-NaF dosage being utilized only for Ki-driven bone segmentation. The ^{18}F-FDG:^{18}F-NaF dosage ratio was optimized with a series of rabbit studies to determine the minimum ^{18}F-NaF dosage necessary for robust K_i-driven bone segmentation without significantly contaminating the ^{18}F-FDG uptake in the targeted regions of interest (ROIs).

The bone tissues were segmented by thresholding the gPatlak K_i image, as estimated from the dynamic ^{18}F-FDG:^{18}F-NaF images (Fig. 1d, left). The same dynamic frame sequence and Dixon-based 4-class MR-AC of the first protocol were employed. However, only for this protocol and for scan fields-of-view (FOVs) that include the brain cortex, any voxels with SUVs, at 60-90min p.i., higher than an empirical upper threshold of SUV=6 were excluded from the K_i-segmented bone mask, as they were exclusively associated with the human brain cortex in all human exams of this study (Fig. 1d, right).

Hybrid PET/MR-AC of ^{18}F-FDG and ^{18}F-NaF PET by delaying the ^{18}F-NaF administration

The third PET/MR protocol involved administration of an ^{18}F-NaF dosage 90 min after an equal ^{18}F-FDG dosage (R1:1) and a 90 min scan commencing 75 min after ^{18}F-FDG injection (Fig. 1c). Thus, the 5-class K_i/MR-AC of net ^{18}F-FDG data prior to ^{18}F-NaF administration becomes possible. Moreover, the independent 5-class K_i/MR-AC of both ^{18}F-FDG and ^{18}F-FDG data for dual-tracer studies can be attained with this protocol. A sequence of 3×5 min ^{18}F-FDG images from the first 15 min and a population-based ^{18}F-FDG IF model (33), to infer the missing IF data of the first 75 min post ^{18}F-FDG injection, were fitted to the gPatlak model to estimate the ^{18}F-FDG K_i, V and k_{loss} images.

The fitted IF and ^{18}F-FDG gPatlak parameters were then utilized to predict, according to the gPatlak method, the net dynamic ^{18}F-FDG distribution after the ^{18}F-NaF injection (last 75min of scan).

To construct the carotid ^{18}F-FDG IF model, we extracted a set of six ^{18}F-FDG human carotid image-derived IFs (IDIFs) from the respective set of dynamic ^{18}F-FDG PET/MR carotid 90min scans of cohort A subjects with no prior indication of carotid atherosclerosis disease (CAD) to minimize contaminating the IDIF measurements with signal from atherosclerotic plaques in the carotid walls. The IDIFs were drawn from blood pool ROIs placed in the lumen of the common carotid sections and as distant as possible from the carotid walls and the bifurcations to further minimize potential spill-in of activity from atherosclerotic plaques developed in arterial walls. Subsequently, the carotid IDIFs were normalized to the injected dosage of each exam, fitted to the Feng's IF parameterized model (34), shifted in time to match their IF peak post-injection times and averaged together to form a single carotid IF model curve. Subsequently, to estimate the missing early section of the carotid ^{18}F-FDG IF for an R1:1 PET/MR carotid exam, the late section of the modeled IF curve (75-90min post injection) was fitted to the carotid ^{18}F-FDG IDIF measurements of the R1:1 exam as obtained during the same post ^{18}F-FDG injection time window (fist 15min of R1:1 scan) from ROIs drawn on the same common carotid lumen regions as those used for the estimation of the IF model (33). It should be noted that the aforementioned process to extrapolate the IDIF of the R1:1 exams to the early post-injection time window (0-75min post ^{18}F-FDG injection) is required only for the purpose of estimating a single value, namely the time integral of the IDIF from ^{18}F-FDG injection time to the start of the scan 75min later according to the Patlak Eq. (1). As a result the gPatlak method to estimate K_i is expected to be sufficiently robust and less sensitive to potential inaccuracies in the population IF model and spill-in of arterial wall activity. The estimated ^{18}F-FDG IF and gPatlak parameters were then utilized to predict, according to the gPatlak model (Eq. 1), the net dynamic ^{18}F-FDG distribution after the ^{18}F-NaF injection (last 75min of scan).

Meanwhile, the list-mode dual-tracer PET data acquired after the ^{18}F-NaF administration was histogrammed along the same frames sequence relative to ^{18}F-NaF injection time, as in previous protocols, and reconstructed with a 4-class MR-AC map. The previously extrapolated dynamic ^{18}F-FDG images were the subtracted from the corresponding dual-tracer images to estimate the dynamic net ^{18}F-NaF images for the last 75 min. The steps used for building the ^{18}F-FDG IF model were also followed to construct a carotid ^{18}F-NaF IF model from the respective set of six dynamic ^{18}F-NaF PET/MR carotid 90min scans of cohort A subjects. Subsequently, the ^{18}F-NaF IF model curve was fitted to IDIF measurements obtained from the previously estimated ^{18}F-NaF dynamic images of the R1:1 protocol. Then, the fitted

18F-NaF IF and the ^{18}F-NaF dynamic images were used as an input to the gPatlak method to estimate the ^{18}F-NaF K_i image, segment the bone tissues and build the 5-class K_i/MR-AC map. We used a population-based ^{18}F-NaF IF model from IDIF data derived from cohort A subjects without prior CAD indication as the possibility of plaques development in the arterial walls and, thus, of spill-in of arterial wall activity is lower for these subjects.

Finally, the reconstructions of the ^{18}F-FDG and the dual-tracer data, before and after the ^{18}F-NaF administration respectively, were repeated with the 5-class K_i/MR-AC map. We then extrapolated the new ^{18}F-FDG images for the last 75 min of scan and subtracted them from the respective dual-tracer images to estimate the final ^{18}F-NaF images.

Pre-clinical validation of K_i- against CT-driven bone segmentation

The proposed K_i-driven bone segmentation method was validated on two healthy rabbits (4.4 and 5.6kg), with a series of 90 min list-mode PET/CT exams over two weeks in a Siemens Biograph^{TM} mCT (Knoxville, TN, USA) scanner (35) using five administration schemes: ^{18}F-FDG, ^{18}F-NaF or ^{18}F-FDG:^{18}F-NaF dosages at 1:1, 4:1 or 9:1 simultaneously-injected ratios (total dosage: 139 +/- 8 MBq, 3.76 +/- 0.19 mCi). All procedures were in accordance with the ethical standards of the Institutional Animal Care and Use Committee (IACUC) of the Icahn School of Medicine at Mount Sinai.

In order to emulate the effect of discretized multi-tissue class MR-AC maps, we synthesized 4- and 5-class AC maps, for each of the ^{18}F-NaF and 4:1 ^{18}F-FDG:^{18}F-NaF PET/CT scans, by segmenting the continuous CT-AC map and assigning a fixed ACF value to each class (32). The CT-segmented bone mask consisted of all CT-AC voxels with original ACFs higher than 0.105cm^{-1}. Furthermore, we generated a 5-class PET/MR-AC map by applying Ki-driven bone segmentation and assigning the remaining non-bone voxels to the conventional 4 tissue classes according to their CT-AC values. The same ACF value (0.12cm^{-1}) was assigned to both CT- and K_i-segmented bone masks. Next, we evaluated the percentage (%) difference maps between the PET images corrected with each of the different discretized AC maps and a PET image corrected with the gold-standard continuous CT-AC maps. Thus, we compared the effect on PET images of K_i- against CT-driven bone segmentation for the same set of discretized ACFs. The same rabbits underwent a similar series of PET/MR exams (142 +/- 9 MBq, 3.84 +/- 0.22 mCi) using a Siemens Biograph^{TM} mMR (Erlangen, Germany) scanner (36) to determine the minimum ^{18}F-NaF dosage ratio for which K_i-driven bone segmentation was feasible without compromising ^{18}F-FDG bias and noise .

Clinical performance evaluation in carotid PET/MR imaging

The clinical performance of the 5-class K_i/MR-AC methods was evaluated on 11 human volunteers (45 +/- 14 y.o., 86 +/- 14kg, 5 males, 6 females) with no prior indication of atherosclerosis randomly assigned into cohorts A and B of 6 and 5 members, respectively. Cohort A subjects underwent a series of three carotid PET/MR scans within 21 +/- 4 days involving (i) ^{18}F-FDG (171 +/- 10 MBq, 4.62 +/-0.27 mCi), (ii) ^{18}F-NaF (173 +/- 11 MBq, 4.68 +/-0.30 mCi) and (iii) simultaneously injected R4:1 ^{18}F-FDG:^{18}F-NaF (344 +/- 24 MBq, 9.30 +/- 0.65 mCi) dosages. Cohort B subjects underwent an ^{18}F-FDG:^{18}F-NaF R1:1 scan with ^{18}F-NaF administration (181 +/ 11 MBq, 4.90 +/- 0.30 mCi) 90 min after ^{18}F-FDG (179 +/- 10 MBq, 4.84 +/- 0.27 mCi) followed by a ^{18}F-NaF PET/MR scan (178 +/- 17 MBq, 4.81 +/-0.46 mCi)) within 10 +/- 2 days. Subsequently, 5 human subjects (49 +/- 13 y.o., 89 +/- 15kg, 2 males, 3 females) with a prior indication of CAD were assigned to cohort C and underwent the same type of PET/MR scans as the subjects of cohort B: an ^{18}F-FDG:^{18}F-NaF R1:1 PET/MR scan with 18F-NaF (188 +/ 15 MBq, 5.08 +/- 0.41 mCi) administered 90 min after ^{18}F-FDG (183 +/- 13 MBq, 4.95 +/- 0.35 mCi) followed by a ^{18}F-NaF PET/MR scan (180 +/- 17 MBq, 4.86 +/-0.46 mCi) within 10 +/- 2 days. The aim of cohort C was to evaluate the performance of the 5-class K_i/MR-AC methods on carotid plaque SUV quantification for both tracer compounds. In all cases, we performed a standard MR-Dixon, a 3D Time-of-Flight MR angiogram, T1-, T2-weighted and proton density turbo spin echo sequences. The study was approved by the institutional review board ethics committee, and informed consent was signed by all enrolled subjects.

A total of 108 carotid wall and adjacent vertebral bone regions were assessed. Specifically, in the ^{18}F-NaF studies of cohort A, the target-to-background (TBR) scores were evaluated for 12 carotid wall regions (at the right and left bifurcation of each subject) and 12 adjacent vertebral bone lesions (2 per subject) between ^{18}F-NaF images corrected with 4- versus 5-class K_i/MR-AC. The analysis was then repeated for the R4:1 ^{18}F-FDG:^{18}F-NaF images of the same subjects cohort at the same 24 regions. In cohorts B and C, the TBR analysis was conducted in the ^{18}F-FDG and ^{18}F-NaF co-registered images for three regions per subject: the carotid wall regions at the right and left bifurcation and one adjacent vertebral bone tissue (15 regions per cohort per tracer).

The carotid TBR scores were evaluated by averaging across the maximum SUV per transaxial slice of a target ROI at the left or right bifurcation and then dividing by the mean SUV of a background ROI at the respective common carotid section. The TBR scores in an adjacent vertebral bone tissue were evaluated by dividing the max SUV of a

large cervical vertebra ROI over the mean SUV of a background ROI at an adjacent soft-tissue region. All ROIs were manually drawn as ellipsoids from the coregistered MR angiograms at matched locations. The influence of partial-volume spill-over effects from the hot target to the surrounding warm background regions were mitigated by evaluating the maximum, instead of the mean, SUVs per slice in the target ROIs, over regions of relatively large surface (bifurcations, common carotids and larger vertebrae). Finally, two-tailed paired t-tests were conducted for each TBR comparison. A value of $p<0.05$ was considered significant.

Results

Evaluation of different ratios of simultaneously-injected ^{18}F-FDG:^{18}F-NaF dosages in PET/CT and PET/MR studies of the same rabbit showed that all ratios ≤ 4:1 triggered distinctively higher vertebral bone K_i scores, relative to ^{18}F-FDG, thus suggesting an optimal ratio of 4:1 for bone segmentation (Fig. 2).

Moreover, the PET/CT results in Fig. 3 from the same rabbit illustrated the satisfactory alignment between continuous CT-AC (gold-standard) and K_i-segmented AC bone maps from ^{18}F-NaF or simultaneously-injected ^{18}F-FDG:^{18}F-NaF ≤ 4:1 ratios. For the same data, we calculated PET bias maps (Fig. 4), displaying the % SUV difference, with respect to PET images corrected with continuous CT-AC maps (gold standard), of PET images corrected with 4- and 5-class segmented CT-AC maps and with proposed 5-class K_i/CT-AC maps (gPatlak K_i-segmented bone defined as fifth tissue class). Our results showed that the mean SUV % bias was reduced by 17.6 +/- 6.3% (^{18}F-NaF) and 15.4 +/- 5.7% (^{18}F-FDG:^{18}F-NaF R4:1) at the arrow-designated vertebral bone regions with 5-class K_i/CT-AC versus 4-class CT-AC. At the same regions, the 5-class K_i/CT-AC yielded similar SUV_{mean} uptake values to those of 5-class CT-AC (difference of -0.4 +/- 2.5% for ^{18}F-NaF and 1.2% +/- 1.5% for ^{18}F-FDG:^{18}F-NaF R4:1), thus suggesting a satisfactory accuracy for K_i-driven bone segmentation.

Fig. 5 illustrates the superior accuracy of K_i- vs. SUV-driven bone segmentation in ^{18}F-NaF PET/MR studies, due to the higher bone-to-soft-tissue K_i contrast. Moreover, similar results were observed with the R4:1 ^{18}F-FDG:^{18}F-NaF simultaneous injection protocol, thereby indicating the feasibility of utilizing the proposed K_i/MR-AC method for ^{18}F-FDG PET/MR studies as well.

In the human carotid ^{18}F-NaF PET/MR images presented in Fig. 6, we observed an ^{18}F-NaF TBR average increase of 17.7% ($p=0.009$) in the carotid bifurcations wall and 20% ($p=0.004$) in the vertebral bones with 5-class K_i/MR-AC versus 4-class MR-AC. The respective TBR enhancements were reduced to 11.5% ($p=0.025$) and 14.9% ($p=0.027$)

when SUV images were used instead as the bone segmentation criterion (SUV/MR-AC). Regarding the ^{18}F-FDG:^{18}F-NaF R4:1 simultaneous administration protocol, we observed in Fig. 7 a TBR average increase of 12.2% (p=0.032) at the left and right carotid bifurcations and 19.9% (p=0.006) at the adjacent vertebral bone regions with 5-class K_i/MR-AC vs. 4-class MR-AC.

In Fig. 8, we demonstrated the feasibility of applying 5-class K_i/MR-AC to ^{18}F-FDG and ^{18}F-NaF carotid data from the same scan as performed on human subjects without prior indication for CAD by using the R1:1 ^{18}F-FDG:^{18}F-NaF PET/MR protocol with delayed ^{18}F-NaF administration 90min post ^{18}F-FDG administration. The bifurcations' mild contrast accords well with literature for ^{18}F-FDG (TBR<1.9) and ^{18}F-NaF (TBR<1.6) in healthy subjects (24, 26). The mean TBR increase in the left and right carotid bifurcations was 15.3% (p=0.009) and 15.5% (p=0.002) for ^{18}F-FDG and ^{18}F-NaF images, respectively. The respective TBR increase in three adjacent vertebral bone regions was 21.6% (p=0.004) for ^{18}F-FDG and 22.5% (p=0.002) for ^{18}F-NaF.

Finally, in Fig. 9, we repeated the same clinical evaluation of the performance of 5-class K_i/MR-AC method using the same R1:1 ^{18}F-FDG:^{18}F-NaF PET/MR protocol but on human carotid data acquired from human subjects with prior indication for CAD (cohort C). In this case, the average contrast at the carotid bifurcations, regardless of the applied AC method, was higher than 2 in accordance with TBR criteria established in literature (24, 26). Both the ^{18}F-FDG and ^{18}F-NaF TBR was increased at the carotid bifurcations and vertebral bones with the 5-class Ki/MR-AC method against 4-class MR-AC. No significant differences were observed in the respective TBR enhancements between subject with and without prior CAD indication.

Discussion

PET bone quantification accuracy attained with 5-class AC maps consisting of K_i-segmented bones and CT-segmented air, lungs and soft tissue classes (5-class K_i/CT-AC) was similar to that attained with CT-segmented air, lungs, soft-tissue and bones (5-class CT/AC) in a series of PET/CT studies of the same rabbit. Moreover, 5-class K_i/CT-AC achieved significantly smaller PET bias in rabbit bone tissues compared to the 4-class CT-AC where bone was segmented as soft-tissue. Furthermore, in all human carotid PET/MR studies, we observed significant TBR increase in both ^{18}F-NaF and ^{18}F-FDG lesions at vertebral bones and at the adjacent carotid bifurcations for the 5-class K_i/MR-AC versus 4-class MR-AC. This is attributed to the larger percentage recovery of the attenuated PET signal in the target regions (vertebral bones and carotid bifurcations) compared to their background tissues (adjacent-to-bone

soft-tissue and common carotid sections, respectively) ROIs, due to the closer proximity of the target lesions to the highly attenuating cortical bone tissues. Past PET/MR studies reported significant PET quantification errors due to misregistration of bone as soft-tissue only for regions in close proximity to the misregistered bone tissue (37). It should be noted that PET partial volume effects (PVE) in a target region are determined by the size of the targeted region with respect to the spatial resolution of the PET scanner. Thus, the same degree of PVE is expected in the target regions before and after the inclusion of the Ki-segmented bone mask in the AC maps. Therefore, the observed TBR increase in the bones and carotid bifurcation walls is not expected to be affected by PVE.

Furthermore, a comparable K_i-driven bone segmentation performance was observed between the rabbit and human studies for the same K_i threshold criteria and ^{18}F-FDG: ^{18}F-NaF dosage ratio, which allowed the optimization of the clinical K_i/MR-AC protocols based on our preclinical findings. The high accuracy in K_i-driven bone segmentation in the rabbits was achieved thanks to the sufficient bone-to-soft-tissue contrast-to-noise ratio (CNR) attained in the rabbit studies, which remained high despite partial contrast losses expected by PVE due to imaging of small bone tissues of rabbits with a human PET/MR scanner of low spatial resolution. The enhanced bone-to-soft-tissue CNR is attributed to the high dosage / weight ratios utilized in the rabbit studies to reduce the noise levels and thus enhance the bone-to-soft-tissue CNR.

Although the ^{18}F-NaF SUV has previously been used for bone segmentation, its dependence on the acquisition timing window and the IF may limit its robustness as a segmentation criterion (20). Furthermore, our results indicated significantly reduced bone-to-soft-tissue TBR for ^{18}F-NaF SUV versus ^{18}F-NaF K_i (-68 +/- 11%, p=0.009) and ^{18}F-FDG:^{18}F-NaF R4:1 K_i (-47 +/- 16%, p=0.037) images, therefore, hampering segmentation accuracy (Fig. 5) and PET quantification (Fig. 6). Alternatively, static ^{18}F-NaF could have been used to derive K_i, but only if the IF and V parameters were known *a-priori*, which is not possible for prospective studies (38).

The gPatlak K_i imaging method was selected to account for the mildly positive tracer uptake reversibility ($k_{loss} \geq 0$, Eq. 1), as suggested by the progressively reduced bone uptake rate constant K_i measured from later time windows (Fig. 2). This method had previously demonstrated enhanced ^{18}F-FDG K_i accuracy and reproducibility, compared to standard Patlak (22), and was chosen to ensure a more accurate K_i-driven bone segmentation.

Our first protocol is streamlined for clinically adoptable bone segmentation but is limited to ^{18}F-NaF-only studies. To support K_i/MR-driven AC for the widely established ^{18}F-FDG tracer, we proposed simultaneously administering ^{18}F-FDG and ^{18}F-NaF at 4:1 ratio, without increasing the total dosage, which produced sufficient bone-to-soft-tissue

contrast for bone segmentation and satisfactory ^{18}F-FDG quantification. However dosage ratio optimization is required to ensure the reliable K_i-driven bone segmentation across multiple human body regions, thus raising the complexity, while ^{18}F-FDG bias may be introduced, if the ^{18}F-NaF contribution to the total uptake is non-negligible at the target regions. On the other hand, regions that are expected to exhibit high 18F-FDG SUV and K_i scores due to considerable metabolic of inflammatory activity, such as the brain cortex or the liver (Fig 3) may be misclassified as bones with K_i-driven bone segmentation thereby affecting 18F-FDG quantification through erroneous attenuation correction. This limitation may in some cases be addressed with a complementary SUV-based bone segmentation criterion, as it was the case with our proposed R4:1 protocol for head-and-neck scans to avoid the brain cortex from being segmented as bone, due to the high K_i values triggered in that region after the simultaneous administration of ^{18}F-FDG and ^{18}F-NaF compounds. However, other regions can be associated with different ^{18}F-FDG and ^{18}F-NaF kinetic properties and, thus, the suggested SUV criterion may be different or unnecessary. Despite that SUV>6 scores were only associated with the brain cortex tissue in all our PET/MR studies scanned with the R4:1 protocol, the possibility for a bone region exhibiting SUV>6 scores and, thus, not being segmented as bone cannot be excluded.

Our third protocol may address these limitations by delaying ^{18}F-NaF administration for 90 min after an equal ^{18}F-FDG dosage, using the same total dosage with previous protocols, to distinguish between the two compounds and apply K_i/MR-AC to each (30). This approach can be clinically useful for PET/MR cardiovascular studies aiming at quantification of inflammation (^{18}F-FDG) only (24, 25) or both inflammation and micro-calcification (^{18}F-NaF) (26-28) in carotid walls with a single PET/MR exam (30). This method requires relatively longer total PET scan times and two separate injections which, nevertheless, can be accommodated nowadays by simultaneous PET/MR scans and automated injection mechanisms. Moreover, the image-based subtraction employed for ^{18}F-NaF estimation may lead to erroneous estimates at high noise levels. Nevertheless, despite the reduction of ^{18}F-FDG and ^{18}F-NaF dosages to half of the standard dosage, relatively low PET noise levels would be expected for both radiotracers, thanks to the small attenuating tissue volume surrounding the carotids, the long PET acquisition times afforded in PET/MR during the similarly long parallel MR sequences and the enhanced sensitivity of the Biograph mMR large axial field-of-view (36). Although K_i-driven bone segmentation relies on gPatlak analysis of PET and IF data initially corrected with sub-optimal 4-class MR-AC, no significant differences were observed in the accuracy of the Ki-driven segmentation of rabbit bone tissues using either 4-class or 5-class CT-AC maps. Furthermore, any effects on K_i estimation accuracy from the use of 4-class MR-AC was systematic across all rabbit exams and a single adjustment in the K_i threshold was

sufficient to account for that bias in all rabbit studies. This is attributed to the sufficient bone-to-soft-tissue contrast attained with both AC methods allowing for the satisfactory alignment between K_i- and CT-derived bone masks in rabbit PET/CT studies even with the sub-optimal 4-class AC method. The use of a single K_i bone segmentation threshold was sufficient to attain similar TBR enhancements with low variance across all human subject studies thereby suggesting that K_i-driven bone segmentation from 4-clas MR-AC maps can be reliable in human PET/MR scans as well. Finally, it is important to note that atherosclerotic plaques may exhibit calcification resulting in increased ^{18}F-NaF uptake (30). Nevertheless, none of the K_i voxel values in the carotid bifurcation walls exceeded the threshold value required to be segmented as bone tissue for any of the enrolled human subjects regardless of prior CAD indication or administration protocol. Thus, the K_i-driven bone segmentation and the PET quantification attained with the hybrid K_i/MR-AC method were not affected by the presence of calcification in carotid walls. However, this is an effect that we plan to monitor in future when applying the proposed AC method to a larger number of subjects and for a wider range of non-bone target regions where calcification is expected, including atherosclerotic plaques in the aorta and coronary arteries.

This proof-of-concept study was focusing on cardiovascular studies and, as such, it was limited to ^{18}F-FDG and ^{18}F-NaF PET uptake evaluations in the carotid bifurcations and neighboring vertebral bone tissue to assess any quantification benefits from including K_i-segmented bone tissue in the absence of CT measurements. Based on previous studies and our results here, which suggested no significant quantification effects in lesions distant to bones when the bone ACFs are neglected (4-class MR-AC), the proposed methods were not evaluated for cardiac PET regions (37). In addition, no significant correlation was found between the CT-derived bone density and the PET-derived bone K_i values. This can be attributed to the lower resolution of PET vs. CT and the PET partial volume effects expected in the small vertebral bone regions preventing the PET signal discrimination across neighboring bone tissue regions of different density. In future, we plan to evaluate 5-class PET/MR-AC methods for larger patient cohorts, dynamic whole-body PET protocols of larger axial FOVs to investigate any quantification benefits for more regions adjacent to bones (39) and for a larger range of bone densities, as well as direct gPatlak K_i reconstruction for improved bone segmentation from PET images with lower noise levels (40).

Our results indicate that 5-class K_i/MR-AC may significantly improve PET quantification and contrast in lesions and regions lying at or closely adjacent to bones, including carotid bifurcations. Furthermore, the presented AC methods have been designed and evaluated for two widely employed PET radiotracers in cardiovascular and oncologic

imaging. Current state-of-the-art clinical PET systems may readily adopt whole-body K_i-driven bone segmentation thanks to their support of whole-body Patlak imaging methods (40). Moreover, the bone AC maps are applied to the same PET data from which they are estimated to ensure accurate co-registration between the two datasets. Finally, K_i/MR-AC methods can be retrospectively applied to previously acquired PET/MR studies, if dynamic PET data are available, and do not require atlas-based bone registrations or additional MR resources.

New knowledge gained

In this study we validated a novel PET-driven bone segmentation method from Patlak K_i imaging. Furthermore, we combined the segmented bones with standard 4-class MR-AC maps to enable 5-class AC in cardiovascular PET/MR studies and showed significant enhancements in ^{18}F-NaF and/or ^{18}F-FDG contrast and quantification at human vertebral bones and carotids.

Conclusion

We proposed a robust and clinically adoptable method for Patlak K_i-driven segmentation of human cortical bone tissues from 18F-NaF or dual-tracer ^{18}F-FDG:^{18}F-NaF PET data without the need for additional bone atlases or MR resources. The K_i-segmented bone tissues can then be combined with standard 4-class MR-AC to significantly enhance ^{18}F-NaF and/or ^{18}F-FDG lesions contrast and quantification at or adjacent to bones in clinical PET/MR studies.

References

1. Zaidi H, Karakatsanis N**.** Towards enhanced PET quantification in clinical oncology. Br J Radiol. 2018;91(1081):20170508.

2. Hendel RC**.** The value and appropriateness of positron emission tomography: an evolving tale. J Nucl Cardiol. 2015;22(1):16-21.

3. Masuda A, Nemoto A, Takeishi Y**.** Technical aspects of cardiac PET/MRI. J Nucl Cardiol. 2018;25(3):1023-8.

4. Nekolla SG, Martinez-Moller A**.** Attenuation correction in cardiac PET: To raise awareness for a problem which is as old as PET/CT. J Nucl Cardiol. 2015;22(6):1296-9.

5. Mok GSP, Ho CYT, Yang BH, Wu TH**.** Interpolated average CT for cardiac PET/CT attenuation correction. J Nucl Cardiol. 2016;23(5):1072-9.

6. Judenhofer MS, Wehrl HF, Newport DF, Catana C, Siegel SB, Becker M, et al. Simultaneous PET-MRI: a new approach for functional and morphological imaging. Nat Med. 2008;14(4):459-65.

7. Lairez O, Robson PM, Fayad ZA**.** Time to move to PET-MR for cardiovascular imaging. J Nucl Cardiol. 2016;23(5):1112-3.

8. Schindler TH**.** Cardiovascular PET/MR imaging: Quo Vadis? J Nucl Cardiol. 2017;24(3):1007-18.

9. Rischpler C, Langwieser N, Nekolla SG**.** Cardiac PET/MRI enters the clinical arena! Finally. J Nucl Cardiol. 2018;25(3):795-6.

10. Nekolla SG, Cabello J**.** The foundation layer of quantitative cardiac PET/MRI: Attenuation correction. Again. J Nucl Cardiol. 2017;24(3):847-50.

11. Lau JMC, Laforest R, Sotoudeh H, Nie X, Sharma S, McConathy J, et al. Evaluation of attenuation correction in cardiac PET using PET/MR. J Nucl Cardiol. 2017;24(3):839-46.

12. Zaidi H, Nkoulou R**.** Artifact-free quantitative cardiovascular PET/MR imaging: An impossible dream? J Nucl Cardiol. 2018.

13. Martinez-Moller A, Souvatzoglou M, Delso G, Bundschuh RA, Chefd'hotel C, Ziegler SI, et al. Tissue classification as a potential approach for attenuation correction in whole-body PET/MRI: evaluation with PET/CT data. J Nucl Med. 2009;50(4):520-6.

14. Paulus DH, Quick HH, Geppert C, Fenchel M, Zhan Y, Hermosillo G, et al. Whole-Body PET/MR Imaging: Quantitative Evaluation of a Novel Model-Based MR Attenuation Correction Method Including Bone. J Nucl Med. 2015;56(7):1061-6.

15. Oehmigen M, Lindemann ME, Gratz M, Kirchner J, Ruhlmann V, Umutlu L, et al. Impact of improved attenuation correction featuring a bone atlas and truncation correction on PET quantification in whole-body PET/MR. Eur J Nucl Med Mol Imaging. 2018;45(4):642-53.

16. Chen KT, Izquierdo-Garcia D, Poynton CB, Chonde DB, Catana C**.** On the accuracy and reproducibility of a novel probabilistic atlas-based generation for calculation of head attenuation maps on integrated PET/MR scanners. Eur J Nucl Med Mol Imaging. 2017;44(3):398-407.

17. Keereman V, Fierens Y, Broux T, De Deene Y, Lonneux M, Vandenberghe S. MRI-Based Attenuation Correction for PET/MRI Using Ultrashort Echo Time Sequences. J Nucl Med. 2010;51(5):812-8.

18. Aasheim LB, Karlberg A, Goa PE, Haberg A, Sorhaug S, Fagerli UM, et al. PET/MR brain imaging: evaluation of clinical UTE-based attenuation correction. Eur J Nucl Med Mol Imaging. 2015;42(9):1439-46.

19. Wong KK, Piert M. Dynamic bone imaging with 99mTc-labeled diphosphonates and 18F-NaF: mechanisms and applications. J Nucl Med. 2013;54(4):590-9.

20. Schramm G, Maus J, Hofheinz F, Petr J, Lougovski A, Beuthien-Baumann B, et al. Correction of quantification errors in pelvic and spinal lesions caused by ignoring higher photon attenuation of bone in [18F]NaF PET/MR. Med Phys. 2015;42(11):6468-76.

21. Patlak CS, Blasberg RG. Graphical evaluation of blood-to-brain transfer constants from multiple-time uptake data. Generalizations. J Cereb Blood Flow Metab. 1985;5(4):584-90.

22. Karakatsanis NA, Zhou Y, Lodge MA, Casey ME, Wahl RL, Zaidi H, et al. Generalized whole-body Patlak parametric imaging for enhanced quantification in clinical PET. Phys Med Biol. 2015;60(22):8643-73.

23. Karakatsanis NA, Abgral R, Boeykens G, Dweck MR, Robson PM, Trivieri MG, et al. 18F-FDG: 18F-NaF PET/MR multi-parametric imaging with kinetics-based bone segmentation for enhanced dual-tracer PET quantification. IEEE Nucl Sci Symp Med Imaging Conf, 2016. 1-5.

24. van der Valk FM, Verweij SL, Zwinderman KA, Strang AC, Kaiser Y, Marquering HA, et al. Thresholds for Arterial Wall Inflammation Quantified by (18)F-FDG PET Imaging: Implications for Vascular Interventional Studies. JACC Cardiovasc Imaging. 2016;9(10):1198-207.

25. Johnsrud K, Skagen K, Seierstad T, Skjelland M, Russell D, Revheim ME. (18)F-FDG PET/CT for the quantification of inflammation in large carotid artery plaques. J Nucl Cardiol. 2017.

26. Irkle A, Vesey AT, Lewis DY, Skepper JN, Bird JL, Dweck MR, et al. Identifying active vascular microcalcification by (18)F-sodium fluoride positron emission tomography. Nat Commun. 2015;6:7495.

27. Hop H, de Boer SA, Reijrink M, Kamphuisen PW, de Borst MH, Pol RA, et al. (18)F-sodium fluoride positron emission tomography assessed microcalcifications in culprit and non-culprit human carotid plaques. J Nucl Cardiol. 2018.

28. Ferreira MJV, Oliveira-Santos M, Silva R, Gomes A, Ferreira N, Abrunhosa A, et al. Assessment of atherosclerotic plaque calcification using F18-NaF PET-CT. J Nucl Cardiol. 2018;25(5):1733-41.

29. Hyafil F, Ferrag W, Kefti C, Le Guludec D. Fluoride imaging of atherosclerotic plaques: Moving from macro to microcalcifications? J Nucl Cardiol. 2018.

30. Karakatsanis N, Trivieri M, Dweck M, Robson P, Abgral R, Soler R, et al. Simultaneous assessment of carotid plaque inflammation and micro-calcification with dual-tracer 18F-FDG: 18F-NaF PET-MR imaging: a clinical feasibility study. J Nucl Med. 2017;58(suppl 1):446-.

31. Boellaard R, O'Doherty MJ, Weber WA, Mottaghy FM, Lonsdale MN, Stroobants SG, et al. FDG PET and PET/CT: EANM procedure guidelines for tumour PET imaging: version 1.0. Eur J Nucl Med Mol Imaging. 2010;37(1):181-200.

32. Ouyang J, Chun SY, Petibon Y, Bonab AA, Alpert N, Fakhri GE. Bias atlases for segmentation-based PET attenuation correction using PET-CT and MR. IEEE Trans Nucl Sci. 2013;60(5):3373-82.

33. Karakatsanis N, Zhou Y, Lodge M, Casey M, Wahl R, Subramaniam R, et al. Clinical Whole-body PET Patlak imaging 60-90min post-injection employing a population-based input function. J Nucl Med. 2015;56(suppl 3):1786-.

34. Feng D, Huang SC, Wang X. Models for computer simulation studies of input functions for tracer kinetic modeling with positron emission tomography. Int J Biomed Comput. 1993;32(2):95-110.

35. Jakoby BW, Bercier Y, Conti M, Casey ME, Bendriem B, Townsend DW. Physical and clinical performance of the mCT time-of-flight PET/CT scanner. Phys Med Biol. 2011;56(8):2375-89.

36. Delso G, Furst S, Jakoby B, Ladebeck R, Ganter C, Nekolla SG, et al. Performance measurements of the Siemens mMR integrated whole-body PET/MR scanner. J Nucl Med. 2011;52(12):1914-22.

37. Vontobel J, Liga R, Possner M, Clerc OF, Mikulicic F, Veit-Haibach P, et al. MR-based attenuation correction for cardiac FDG PET on a hybrid PET/MRI scanner: comparison with standard CT attenuation correction. Eur J Nucl Med Mol Imaging. 2015;42(10):1574-80.

38. Siddique M, Blake GM, Frost ML, Moore AE, Puri T, Marsden PK, et al. Estimation of regional bone metabolism from whole-body 18F-fluoride PET static images. Eur J Nucl Med Mol Imaging. 2012;39(2):337-43.

39. Karakatsanis NA, Lodge MA, Tahari AK, Zhou Y, Wahl RL, Rahmim A. Dynamic whole-body PET parametric imaging: I. Concept, acquisition protocol optimization and clinical application. Phys Med Biol. 2013;58(20):7391-418.

40. Karakatsanis NA, Casey ME, Lodge MA, Rahmim A, Zaidi H. Whole-body direct 4D parametric PET imaging employing nested generalized Patlak expectation-maximization reconstruction. Phys Med Biol. 2016;61(15):5456-85.

FIGURES AND LEGENDS

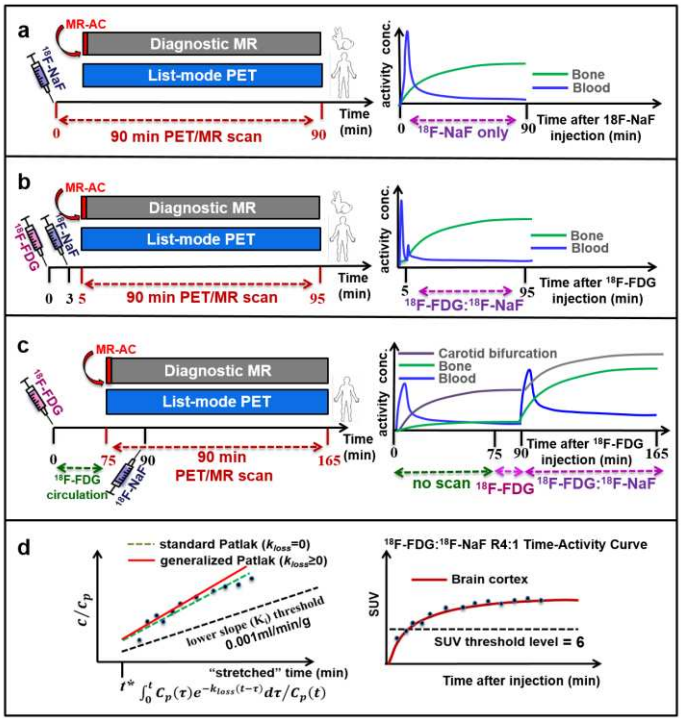

Fig. 1. Illustrative overview of (a) ^{18}F-NaF-only, (b) simultaneous R4:1 ^{18}F-FDG:^{18}F-NaF and (c) R1:1 ^{18}F-FDG with delayed ^{18}F-NaF administration protocols (left column) with their respective dynamic courses of activity concentration in bone and blood (right column). (d) Standard and gPatlak K_i (left) and SUV (right) threshold criteria for PET-driven bone segmentation.

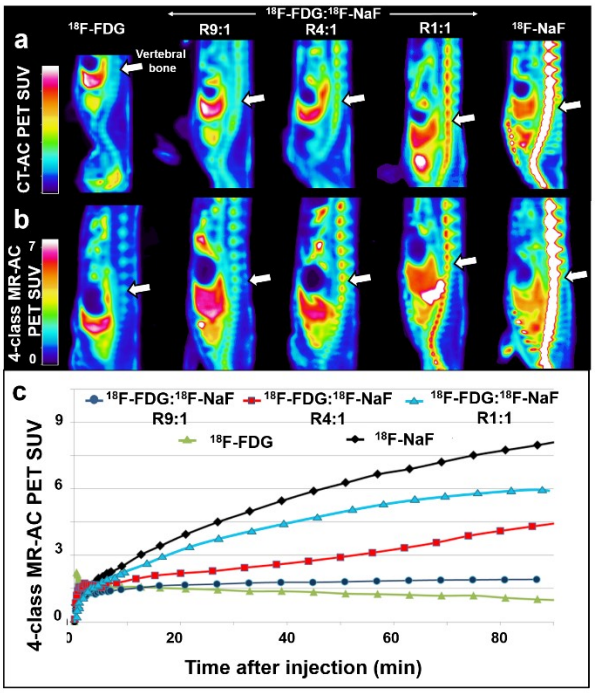

Fig. 2. Preclinical study to optimize the simultaneously injected ^{18}F-FDG:^{18}F-NaF dosage ratio for bone segmentation. Non-registered PET sagittal images from (a) PET/CT and (b) PET/MR data, as acquired from the same rabbit subject on different days at 60-90 min after injection of the same total dosage of either ^{18}F-FDG, ^{18}F-NaF or combined ^{18}F-FDG:^{18}F-NaF (simultaneous injection) at ratios of R9:1, R4:1 and R1:1. (c) Respective time–activity curves from the PET/MR data in the same vertebral bone region (arrows) across the different scans. Similar results were obtained from a wide set of different vertebra regions. The reduced ^{18}F-FDG uptake at later times suggests ^{18}F-FDG uptake reversibility in bones, thereby demonstrating the need for generalized versus standard Patlak K_i imaging. The SUV values in all PET images were calculated based on the total amount of administered dosage.

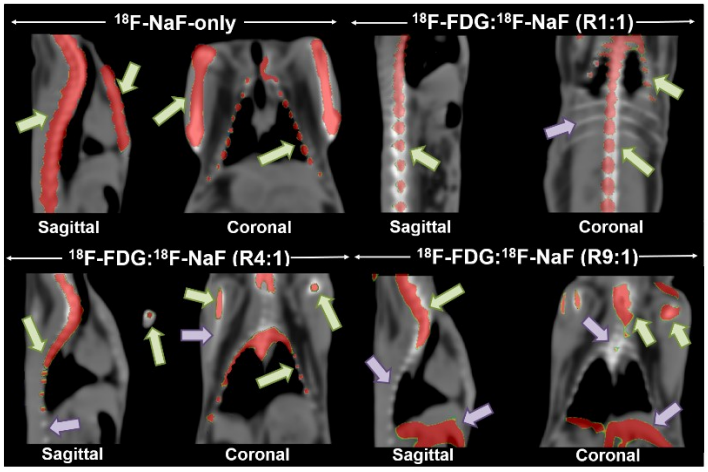

Fig. 3. Coronal and sagittal views of continuous CT-AC maps (gray) fused with the K_i-segmented bone masks (red) from PET/CT scans of the same rabbit with ^{18}F-NaF (upper left) or ^{18}F-FDG:^{18}F-NaF simultaneously-injected dosages at R1:1 (upper right), R4:1 (bottom left) and R9:1 (bottom right) ratios. The arrows indicate areas of satisfactory (green) and non-satisfactory (purple) alignment between CT- and K_i-segmented bone. Note that in case of simultaneously-injected ^{18}F-FDG:^{18}F-NaF dosages administered at ratios higher than 4:1, large non-bone regions with a high ^{18}F-FDG metabolic uptake, such as the liver, are expected to also exhibit a high K_i score and thus be segmented as bone tissue with K_i-driven bone segmentation.

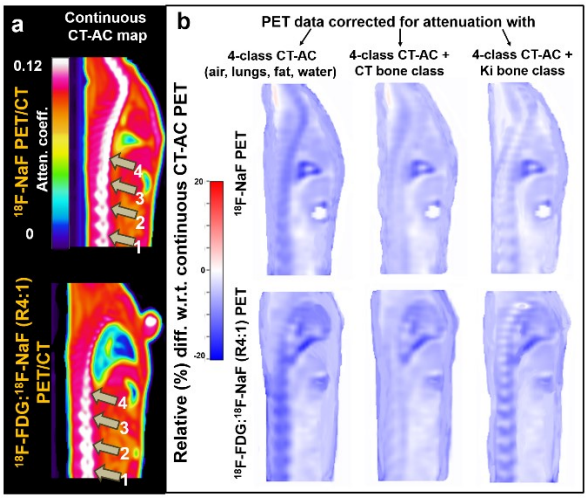

Fig. 4. Rabbit PET/CT validation of K_i-driven bone segmentation: (a) Continuous CT-AC maps for ^{18}F-NaF (up) and ^{18}F-FDG:^{18}F-NaF R4:1 (bottom) protocols. (b) Percentage (%) SUV difference (bias) maps, with respect to continuous CT-AC PET, of PET images corrected with segmented 4-class CT-AC, 4-class CT-AC + CT-segmented bone class (5-class CT-AC) and 4-class CT-AC + K_i-segmented bone class (5-class Ki/CT-AC). Average SUV (SUV_{mean}) and % SUV bias scores were evaluated in the four arrow-designated vertebral bone regions.

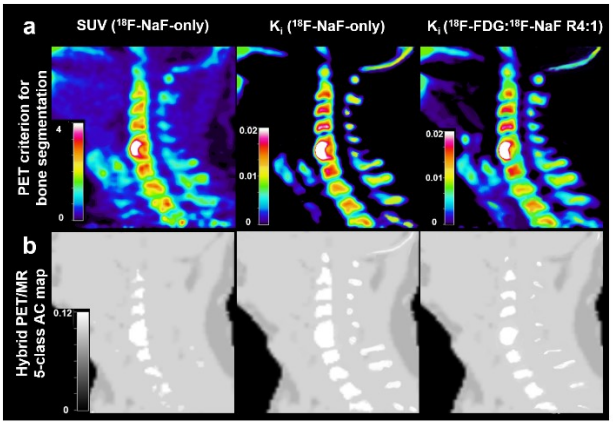

Fig. 5. Clinical demonstration of K_i-driven bone segmentation in a human carotid PET/MR study from a cohort A subject. (a) PET-driven bone segmentation criterion: (left-to-right) ^{18}F-NaF SUV (60-90 min p.i.), ^{18}F-NaF K_i (0-90 min p.i.) and simultaneously-injected ^{18}F-FDG:^{18}F-NaF R4:1 K_i (0-90 min p.i.) (b) Hybrid PET/MR-driven 5-class AC maps using the corresponding PET-driven criterion for bone segmentation.

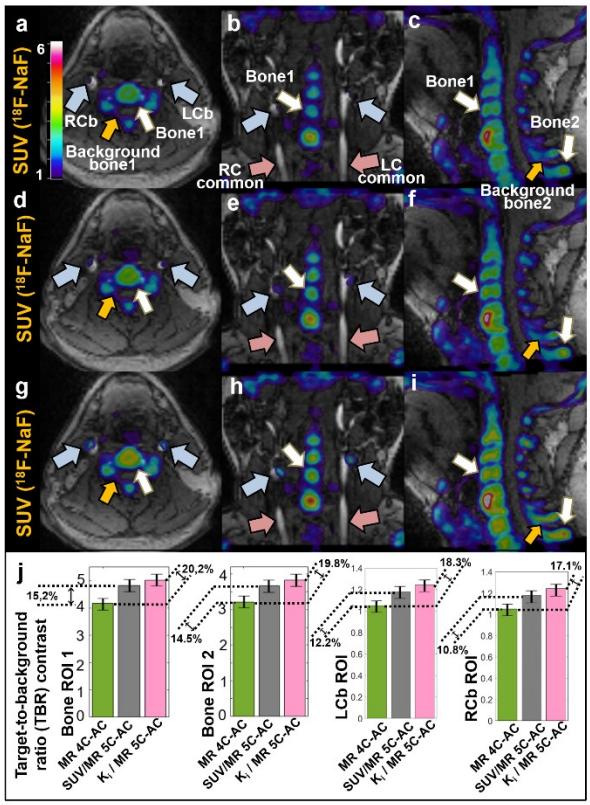

Fig. 6. Clinical evaluation of the 5-class K_i/MR-AC method in human carotid ^{18}F-NaF PET/MR studies from cohort A subjects. (top 3 rows, left-to-right): Transaxial, coronal and sagittal views for a single subject of MR angiogram fused with ^{18}F-NaF SUV images 60-90 min p.i. corrected with (a)-(c) 4-class MR-AC, (d)-(f) 5-class SUV/MR-AC and (g)-(i) 5-class K_i/MR-AC maps. (j) Respective PET TBR scores, averaged across all six subjects of cohort A, at left and right carotid bifurcations (blue arrows) and adjacent bones (white arrows). The carotid and bone background ROIs were drawn at the common left and right carotids (pink arrows) and a soft-tissue region adjacent to the cervical vertebrae (yellow arrows), respectively.

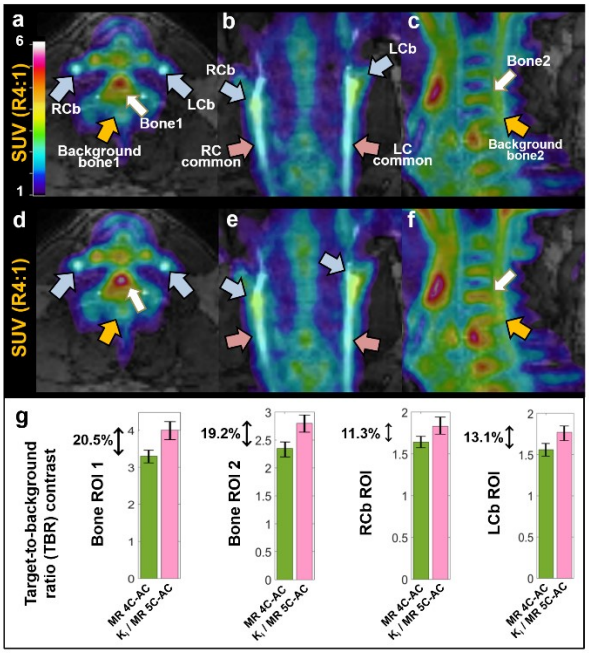

Fig. 7. Clinical evaluation of the 5-class K_i/MR-AC method in human carotid ^{18}F-FDG:^{18}F-NaF (R4:1, simultaneously-injected) studies from cohort A subjects. (top 2 rows, left-to-right) Transaxial, coronal and sagittal views for a single subject of MR angiograms fused with ^{18}F-FDG:^{18}F-NaF PET SUV images 60-90 min p.i. corrected with (a)-(c) 4-class MR-AC and (d)-(f) 5-class K_i/MR-AC maps. (g) Respective PET TBR scores, averaged across all six subjects of cohort A, at left and right carotid bifurcations (blue arrows) and adjacent bones (white arrows). The carotid and bone background ROIs were drawn at the common left and right carotids (pink arrows) and a soft-tissue region adjacent to the cervical vertebrae (yellow arrows), respectively.

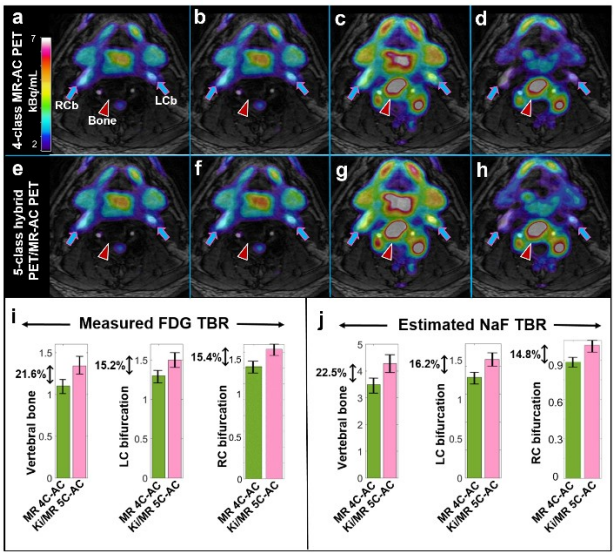

Fig. 8. Clinical evaluation of the 5-class K_i/MR-AC method in human carotid ^{18}F-FDG:^{18}F-NaF (R1:1, delayed ^{18}F-NaF administration by 90min post ^{18}F-FDG administration) studies from cohort B subjects (without prior indication for carotid atherosclerosis). (top 2 rows, left-to-right): Fusion of transaxial MR angiograms with PET images of a single subject corrected with the 4-class AC method. The PET maps represent signal of (a) measured ^{18}F-FDG at 75-90 min post ^{18}F-FDG administration, (b) extrapolated ^{18}F-FDG, (c) measured dual-tracer ^{18}F-FDG:^{18}F-NaF and (d) estimated ^{18}F-NaF at 60-75 min post ^{18}F-NaF administration. (e)-(h) Respective PET/MR fused images corrected with the 5-class K_i/MR-AC method. (Bottom row) TBRs of (i) ^{18}F-FDG at 75-90min post ^{18}F-FDG administration and (j) ^{18}F-NaF at 60-75 min post ^{18}F-NaF administration, averaged across all four subjects of cohort B. The right and left carotid bifurcation (blue arrows) and an adjacent bone region (red arrows) were considered as target ROIs. The carotid and bone background ROIs were drawn at the common left and right carotids and a soft-tissue region adjacent to the cervical vertebrae, respectively.

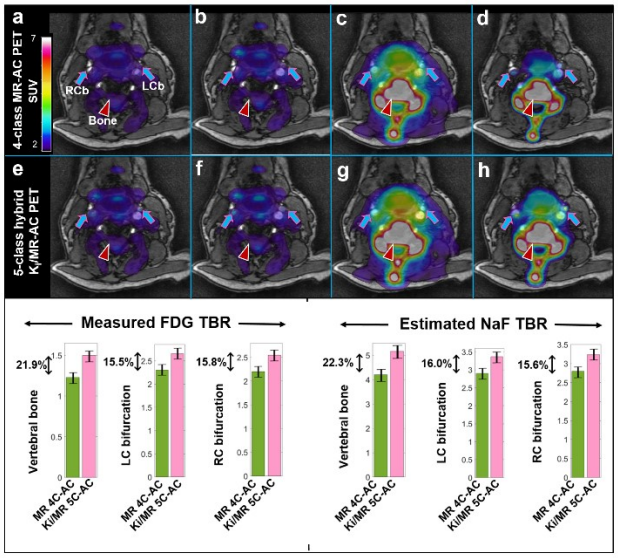

Fig. 9. Same qualitative and TBR evaluation of the 5-class K_i/MR-AC PET against the 4-class MR-AC PET as in Fig. 8 but for human carotid ^{18}F-FDG:^{18}F-NaF (R1:1, delayed ^{18}F-NaF administration by 90min post ^{18}F-FDG administration) studies from cohort C subjects (with prior indication for carotid atherosclerosis).